Changes in membrane dielectric properties of porcine kidney cells provide insight into the antiviral activity of glycine

*Sanaz Habibi,[†] Pratik U. Joshi,[†] Xue Mi,[†] Caryn L. Heldt,[†] and Adrienne R. Minerick[†]**

[†] Department of Chemical Engineering, Michigan Technological University, Houghton, MI, 49931, USA

KEYWORDS: Dielectrophoresis, glycine, antiviral compound, frequency

*e-mail: minerick@mtu.edu

ABSTRACT

The ability to monitor the status and progression of viral infections is important for development and screening of new antiviral drugs. Previous research illustrated that the osmolyte glycine (Gly) reduced porcine parvovirus (PPV) infection in porcine kidney (PK-13) cells by stabilizing the capsid protein and preventing virus capsid assembly into viable virus particles. Dielectrophoresis (DEP) was examined herein as a non-invasive, electric field and frequency-dependent tool for real time monitoring of PK-13 cell responses to obtain information about membrane barrier functionality and polarization. DEP responses of PK-13 cells were compared to PPV-infected cells in the absence and presence of the osmolyte glycine. With infection progression, PK-13 DEP spectra shifted toward lower frequencies reducing crossover frequencies (f_{CO}). The spherical single-shell model was used to extract PK-13 cell dielectric properties. Upon PPV infection, specific membrane capacitance increased over the time progression of virus attachment,

penetration, and capsid protein production and assembly. Following glycine treatment, the DEP spectra displayed attenuated f_{CO} and specific membrane capacitance values shifted back toward uninfected PK-13 cell values. These results suggest that DEP can be used to non-invasively monitor the viral infection cycle as well as screen antiviral compounds. DEP can augment traditional tools by elucidating membrane polarization changes due to drug mechanisms that interrupt the virus infection cycle.

Introduction

In medical care, there is a growing demand for early diagnoses, tailored treatment strategies and monitoring that are less invasive, near real-time and have high accuracy; this is particularly relevant as medical systems globally are grappling with timely diagnoses of novel coronavirus COVID-19. Electrokinetic microfluidic platforms can enable point-of-care diagnostics and pharmaceutical screenings for a breadth of cellular diseases with advantages such as lower patient sample and reagent consumption, lower-cost, shorter response and quantification times, and lower labor demands.[1-3]

Electrokinetic microfluidic platforms enable cell manipulation, characterization, separation, and concentration at the precision of a single cell level.[4-6] A versatile electrokinetic technique is dielectrophoresis (DEP), which can induce directional motion of populations of cells within spatially non-uniform electric fields.[5, 7, 8] One of the main benefits of utilizing DEP is that it is noninvasive to the target cells and does not depend on property-altering fluorescent or magnetic labeling to interrogate cells.[7] DEP responses are directly dependent on ion transport mechanisms leading to charge buildup and cell polarizability based on the applied electric fields.[9] DEP-based microfluidic devices allow (sub)cellular characterization that reveals or exploits the cell's dielectric properties. Monitorable properties include changes in cell morphology, membrane

surface area (e.g. the appearance of microvilli or blebs), membrane conductivity associated with a membrane structural change, and/or cytoplasm conductivity changes associated with ion distributions. All of these cell features impact the cell's dielectrophoretic frequency spectrum that is exclusively characteristic of a particular cell and its health.[10, 11]

A cell's dielectrophoretic behavior provides a variety of useful information about a cell's physiological and pathological status.[12-24] A cell's transition from a healthy to a diseased state is often associated with changes in the cell's dielectric properties. Extensive studies have shown that healthy,[12, 13] drug-treated,[14] parasite-infected,[20, 21] cancerous,[15-17] and virus-infected cells[22-24] exhibit characteristic DEP spectral signatures. The World Health Organization lists viral diseases as an essential *in vitro* diagnostic initiative.[25] During pathogenic viral infection, there are complex cellular changes that occur in the cell, which can be exploited as disease electrophysiological markers to diagnose, track disease progression, and help vet more tailored treatment strategies.[22-24] Although considerable effort has been expended on studying virus-host interactions through traditional pathological techniques[26-28] with a few cell characterizations with DEP,[22-24] clarification is required regarding the membrane-related perturbation kinetics associated with cell membrane dielectric properties during the infection cycle.

This work aims to study the viral infection cycle with non-invasive electrokinetic tools to help elucidate additional mechanistic insights into viral infections. In this study, porcine parvovirus (PPV) was chosen as a model to study the virus infection cycle. PPV is a non-enveloped DNA virus that is responsible for pig intestine infections, which is the most frequent cause of swine reproductive failure.[27] This virus is also often used as a model for the human B19 parvovirus,[29] which is associated with a number of conditions, such as fifth disease in children and arthritis and arthralgias in adults.[30] The PPV infection cycle has been pieced together from traditional

pathological observation techniques.[26-28] Briefly, upon infection, viruses bind to specific target receptors on the cell membrane surface where the parvovirus capsid is internalized through clathrin-coated pits and then transferred through the endocytic path. The capsid is uncoated, and the genome is released and translocated to the nucleus for genome replication, transcription, and protein expression. The viral DNA is replicated, and the expressed genes enable progeny viral genomes to form newly assembled capsids within the nucleus. During post-capsid assembly and genome packaging, newly formed virions exit the nucleus and are transported through the cell membrane.[26, 27]

During the infection process, viruses must overcome numerous cellular barriers to infection, most prominent is the cell membrane.[31, 32] Cell membrane integrity is compromised upon virus penetration;[22-24] mechanisms for non-enveloped virus penetration are less understood than enveloped virus mechanisms.[31, 32] Although a more coherent understanding of this process is starting to emerge through traditional fluorescent tools, non-invasive DEP monitoring can provide further insights into mechanisms during the viral infection cycle. It was shown for a couple enveloped and one non-enveloped viruses that cytoplasmic conductivity and specific membrane capacitance changed over the virus infection cycle.[22-24] Of particular relevance to this study, Petiot et al. showed the cytoplasmic conductivity and the specific membrane capacitance of the non-enveloped reovirus increased by more than 25% during viral component synthesis and assembly of progeny viruses.[24] This work is the first to monitor cell membrane dielectric properties via DEP to yield a better understanding of the trafficking during the non-enveloped virus infection cycle in the presence of antiviral compound.

DEP can also provide insights into the mechanisms of antiviral compounds. Recently, there has been a growing interest in leveraging natural compounds for therapeutics[33] providing a new

class of compounds that would supersede current viral drugs that are losing efficacy.[34] Osmolytes are potential natural antiviral compounds; they are small organic molecules found in cells with the ability to stabilize intracellular proteins against environmental stress, such as extreme temperature or high osmotic pressure.[35] The osmolytes glycine and TMAO demonstrated antiviral efficacy for PPV.[28] It was previously postulated that glycine either disrupted capsid assembly or reduced virus DNA production. This work thus focused on the impact of glycine on membrane-related kinetics of PPV.

DEP cell responses are best observed in microfluidic device platforms as demonstrated previously to screen a plethora of health/unhealthy cell systems, discern biomarker progression and even screen for new drug candidates.[12-24] Our group has optimized frequency sweeps as a tool to generate near continuous DEP spectra.[36, 37] There are distinct advantages to this approach including rapid data acquisition for entire cell populations, which is important when those cell populations are undergoing time-dependent alterations as is the case with the viral infected cells studied herein. Thus, this work explored the use of DEP within a proven microdevice platform[38] to characterize the differences between infected and non-infected cells, as well as how the presence of glycine affected the cell during the infection cycle. We hypothesize that the cell's transition from a healthy to the diseased state in the absence and presence of glycine will alter cell membrane capacitance, which can be discerned from measured DEP spectra. These changes can be used to screen antiviral compounds and supplement traditional tools to more thoroughly elucidate drug mechanisms that interrupt the virus infection cycle.

Dielectrophoresis Theory and Background

Dielectrophoresis employs alternating current (AC) signals to spatially manipulate particles or cells toward high or low electric field regions within a medium. The dielectrophoretic force,

$\vec{F}_{DEP}$, on a homogenous spherical particle (a rough first approximation to a cell), can be described by a volume term reduced 1/3 by the spherical depolarization factor ($4\pi r^3$), a frequency-dependent dielectric term (Re $[f_{CM}]$), and a non-linear electric field term ($\nabla\vec{E}^2{}_{rms}$) as follows:[39]

$$\vec{F}_{DEP} = 4\pi r^3 \varepsilon_m \text{Re}\,[f_{CM}]\nabla\vec{E}^2{}_{rms} \quad (1)$$

where r is the outer particle (or cell) radius, ε_m is medium permittivity, Re $[f_{CM}]$ is the real part of the Clausius–Mossotti factor, and $\nabla\vec{E}^2{}_{rms}$ is the electric field gradient squared. Within non-uniform electric fields, particle motion can be described by the f_{CM}:[40-42]

$$f_{CM} = \frac{\varepsilon_p^* - \varepsilon_m^*}{\varepsilon_p^* + 2\varepsilon_m^*} \qquad \text{where} \qquad \varepsilon_i^* = \varepsilon_i + \frac{\sigma_i}{j\omega} \quad (2)$$

where ε_i^* is the complex permittivity, ε_i is the permittivity, σ_i is the conductivity, and the subscript i represents either the particle ($i = p$) or the medium ($i = m$). The complex permittivity, ε_i^*, is also dependent upon the angular frequency (ω) with j representing the imaginary number ($j = \sqrt{-1}$).[40] When exposed to an electric field, the cell electrically polarizes to form an electric dipole moment. The DEP force depends on the real component of the induced moment while the imaginary part correlates with electrorotation (ROT). ROT utilizes rotating fields and was first demonstrated on biological cell in 1982.[43] ROT, which is a complementary to DEP, is a versatile method for manipulating single cells to measure multiple biophysical properties, but it has limited throughput.[44] In Eq. (2), if the Re $[f_{CM}]$ is positive, the cells move up electric field gradients. This behavior is referred as positive DEP (p-DEP), indicating that the cells are more polarizable than the suspending medium $\varepsilon_p^* > \varepsilon_m^*$.[40] If the Re $[f_{CM}]$ is negative, the cells move down electric field gradients. This is known as negative DEP (n-DEP), reflecting lower cell polarizability than the suspending medium $\varepsilon_p^* < \varepsilon_m^*$.[40] When Re $[f_{CM}]$ is zero, the cell is not polarized and coincides with the frequency at which cells transition from experiencing n-DEP to p-DEP or p-DEP to n-DEP.

This is called the crossover frequency (f_{CO}) and manifests in experiments as little or no motion in the electric field.[42]

The f_{CM} used in the DEP force expression Eq. (1) is fairly accurate in describing homogeneous spherical particles; however, biological cells have more complex heterogeneous structures.[45] Thus, deviation from homogeneity reduces Eq. (1) accuracy. Thus, cell polarization responses can be modeled using a series of equations where the cell's structural complexity is added to the DEP model by introducing structural layers (i.e. cell membrane and cytoplasm). Porcine kidney (PK-13) cells are spherical in shape when in a fluidic suspension as exists in our microfluidic device. Further, PK-13 cells can be approximated as conductive cytoplasm sphere bounded by an insulator-like cell membrane, which can be described by a spherical single-shell model. [40, 42]

In the presence of electric fields, cells exhibit frequency-dependent dielectric dispersions which can be characterized by the α- (sub-Hz to kHz), β- (kHz to MHz), and γ- (MHz to GHz) dispersion regions. Dielectric dispersions originate from electrical polarization at different length-scales of the cellular system; [46] enabling calculation of the cell's dielectric properties. Here, we explore 0.1 to 0.9 MHz in the β-dispersion region where Maxwell-Wagner interfacial polarizations govern cell responses. In this frequency region, the cell's dielectric dispersion is influenced by the interfacial polarization between an insulator-like cell membrane and the medium. A wide range of information can be obtained about a cell population with intact membranes or compromised membranes in this radio frequency region (kHz to MHz).[7, 47] This allows researchers to deduce characteristics of cell damage, apoptosis, necrosis, and drug-induced cell protection or demise from the measured DEP spectra.[7, 48]

DEP experiments are conducted while monitoring via video microscopy the cell's motion as a function of frequency in non-uniform electric fields. The field-induced charge distribution on membrane interfaces changes as the frequency sweeps from high to low values enabling near real-time tracking of interfacial charge polarization/relaxation shifts. Quantification of motion determines DEP dispersion maxima and minima and crossover frequency (f_{CO}); extraction of these features from the DEP spectra enables calculation of cell properties that directly correlate to mechanistic changes.

Quantifying DEP force spectra on bioparticles by velocity tracking measurements

When cell shape and radius are known, the DEP force spectra can be determined by measuring the cell velocity ($\vec{v}$).[49] If Brownian motion and the buoyancy force are neglected, the net DEP force on the cell is the sum of the Stokes drag force ($\vec{F}_D$) and the acceleration force ($\vec{F}_A$): $\vec{F}_{DEP} = \vec{F}_D + \vec{F}_A$. For a spheroidal cell, the DEP force is:[50]

$$\vec{F}_{DEP} = 6\pi\eta r\,\vec{v} + m\vec{a} \tag{3}$$

where η is the fluid's dynamic viscosity and r, $\vec{v}$, m, and $\vec{a}$ are the cell's radius, velocity, mass, and acceleration, respectively. Cell mass was estimated as 10^{-13} kg.[51] In Eq. (3) the mass times acceleration term is negligible because $\vec{F}_A$ is five orders of magnitude smaller that $\vec{F}_D$.[44, 52] This reduces Eq. (3) to $\vec{F}_{DEP} = \vec{F}_D = 6\pi\eta r\,\vec{v}$. The viscosity of phosphate buffer saline (PBS), a water-based salt solution, was assumed to be that of liquid water (1 cP at 20 ºC). Crossover frequency (f_{CO}) was visualized via video microscopy and subsequently discerned from the DEP spectra because it is the cell's transition from n-DEP to p-DEP in this frequency range. This zero-polarization state can be calculated by f_{CO}:[7, 53]

$$f_{CO} = \frac{1}{\sqrt{2}}\frac{\sigma_m}{\pi r C_{mem}}\sqrt{1 - \frac{rG_{mem}}{2\sigma_m} - 2\left[\frac{rG_{mem}}{\sigma_m}\right]^2} \tag{4}$$

where C_{mem} and G_{mem} are the specific membrane capacitance and conductance, respectively and are given by $C_{mem} = \varepsilon_{mem}/d$ and $G_{mem} = \sigma_{mem}/d$.[53] As the DEP force changes polarity, the cell's dielectric properties (i.e. specific membrane capacitance and conductance) can be estimated from observed crossover frequency (f_{CO}) and the remaining DEP spectra. In Eq. (4), the medium dielectric properties are known and can be controlled. Once the f_{CO} is determined experimentally, the membrane capacitance and conductance can be calculated. The membrane capacitance term reflects how strongly the membrane acts as a charge barrier and is a function of membrane area, thickness, composition/dielectric properties, and morphological complexity. Membrane conductance reflects the net transport of ionic species across the membrane through pores, ion channels, and defects under the influence of an applied field. Each cell has a unique dielectrophoretic spectrum as a function of frequency that reflects the molecular structure and dielectric properties of both the cell's surface and internal structure. The practical applications of observing the DEP spectra include being able to determine the cell dielectric properties resulting from membrane damage, apoptosis, necrosis, and drug-induced cell protection or demise.

The interfacial polarization between the medium and cytoplasm interface can result in a second DEP crossover (f_{CO_2}) which depends on the cytoplasm conductivity and permittivity.[54, 55] The primary goal was to study the physical mechanism by which PPV penetrates the membrane. Thus, DEP responses were recorded from 0.1 to 0.9 MHz over 10 hours.

In summary, this work utilizes DEP-based microfluidics as a label-free platform to characterize porcine kidney cells during various time points of the PPV infection cycle and to ascertain effects from an antiviral compound, glycine. DEP spectra were compiled from cell trajectories and velocity within a microfluidic device to determine DEP force spectra and f_{CO}. Data was collected while applying a 0.1 V_{pp}/μm signal with 0.1-0.9 MHz frequencies at 0, 1.5, 4, 8, and 10 hpi in the

absence and presence of glycine. Models were fit to the DEP spectra in order to back out cellular properties.

Materials and Methods

Chemicals and preparation

Porcine kidney cells (PK-13, CRL-6489) were purchased from ATCC (Manassas, VA, USA). Eagle's minimum essential media (EMEM), sodium bicarbonate (7.5%), phosphate buffered saline (PBS, pH 7.2), penicillin/streptomycin (100X, pen-strep) and trypsin/EDTA (0.25%) for cell propagation were purchased from Life Technologies (Carlsbad, CA, USA). Fetal bovine serum (FBS, Canada origin) was purchased from HyClone™ GE Healthcare (Pittsburg, PA, USA). Potassium phosphate monobasic (ACS grade, ≥99.0%), and potassium phosphate dibasic (ACS grade, ≥99.0%) were purchased from EMD Millipore (Billerica, MA, USA). Sodium chloride (ACS grade, >99.0%) was purchased from Macron Chemicals (Center Valley, PA, USA). Glycine (BioUltra, for molecular biology, ≥99.0%), glutaraldehyde (Grade I, 70% in H2O), and dextrose (≥99.5%) were purchased from Sigma-Aldrich (St. Louis, MO, USA).

All DEP experiments were conducted in controlled isotonic phosphate buffer saline (iPBS) solution adjusted to a conductivity of 0.1 S/m. To prepare iPBS, 2.6 mM potassium phosphate monobasic, 2.6 mM potassium phosphate dibasic, 2.6 mM sodium chloride, and 274.3 mM dextrose were mixed in 24.9 mL E-pure water (18.2 Ω·cm, EMD Millipore Simplicity Ultrapure 185, Billerica, MA, USA) stored at 4°C and used within one week.

Cell culture, virus propagation, and titration

PK-13 cells were grown in EMEM completed with 10% FBS and 1% pen-strep, as previously stated.[28] Porcine parvovirus (PPV) NADL-2 strain was a generous gift from Dr. Ruben Carbonell

from North Carolina State University (Raleigh, NC, USA). PPV was propagated in PK-13 cells as described previously.[56] The PPV titer was determined using the colorimetric MTT cell viability assay as described previously.[56] Briefly, cells were placed in 96-well plates. Virus was added to the cells and serially diluted. After a 5-day incubation, the MTT salt was added to determine cell viability. The dilution that allowed 50% of the cells to survive was denoted as the MTT. Additionally, to determine cell viability, cell membrane integrity was monitored by their ability to exclude trypan blue dye. The trypan blue test has been validated and itself does not induce cell death in a controlled environment.[57]

Virus infection, osmolyte treatment, DEP solution preparation

Multiple flasks of PK-13 cells were cultured for DEP tests, including non-infected (control), PPV-infected, glycine-treated/non-infected (glycine control), and glycine-treated/PPV-infected. Each flask was seeded with 9×10^5 cells and incubated at 37°C, 5% CO_2, and 100% humidity for 48 hours to obtain 70% confluency. To prepare non-infected (control) and PPV-infected flasks, the culture medium was replaced by 1 mL of fresh culture medium and 1 mL of 7 $\log_{10}(MTT_{50}/mL)$ PPV, respectively. For osmolyte treatment, the culture medium was replaced with 1 mL of 0.2 M glycine for glycine-treated/non-infected (glycine control) flasks and 7 $\log_{10}(MTT_{50}/mL)$ PPV containing 0.2 M glycine for glycine-treated/PPV-infected flasks. Flasks were rocked for 1 hour on a Roto-Shake Genie Rocker (Bohemia, NY, USA) to allow a maximum number of the viral particles to attach to the cells. After one hour, 9 mL of fresh culture medium was added to non-infected (control) and PPV-infected flasks while 10 mL of fresh culture media containing 0.2 M glycine was introduced to the non-infected and PPV-infected flasks. To investigate the impact of glycine on the PK-13 cells, the glycine control DEP experiments were conducted, and the DEP response quantified at 0, 1.5, 4, 8, and 10 hours. Four different samples were prepared: non-

infected, PPV-infected, glycine-treated/non-infected, and glycine-treated/PPV-infected PK-13 cells. Non-infected PK-13 cell samples were used as controls for the PPV infection cycle while glycine-treated/non-infected PK-13 samples were utilized as glycine controls.

A standard mammalian cell subculture protocol was implemented to extract the cell monolayer from the flasks prior to the DEP measurement. The culture medium was removed from the incubated flasks. The cells were washed with 3 mL of PBS, then treated with trypsin/EDTA (0.25%) for ~ 5 min to remove the cell monolayer. Next, the cells were suspended in completed EMEM at a 1:1 ratio. The PK-13 cell suspension was transferred to sterile tubes and centrifuged for 3 minutes at 415 relative centrifugal force (rcf) in a Sorvall ST16R centrifuge (Thermo Scientific, Pittsburgh, PA). The supernatant was removed, and the PK-13 cells were resuspended in 500 μL of DEP suspension medium, e.g. iPBS with a 0.1 S/m conductivity.

To inactivate the virus, glutaraldehyde was added to the PPV stock to a final concentration of 1% and incubated for 1 hour at room temperature. The excess glutaraldehyde was removed from the stock using a Biotech Cellulose Ester 1,000 kDa dialysis tubing (Rancho Dominguez, CA, USA) at 4°C with 2 PBS exchanges over 2 days. The inactivation of PPV was confirmed with the MTT assay. To check the robustness of the DEP technique, the inactivated PPV was exposed to PK-13 cells, and the DEP tests were repeated at 0, 1.5, 4, 8, and 10 hours.

Microfluidics design and fabrication

An eight-electrode polynomial design was used to study non-infected and PPV-infected PK-13 cells before and after glycine treatment. Figure 1a shows the schematic of the microfluidic device configuration with a PDMS fluidic layer bonded on a microfabricated Cr/Au electrode glass slide. As shown in Figure 1b, eight triangular electrodes converge symmetrically at a center point enabling symmetric monitoring of cell responses. The shortest and longest distances between the

electrodes are 50 µm and 125 µm, respectively. Photolithography, sputtering, and lift-off were employed to fabricate the microelectrodes on glass microscope slides following previously detailed procedures.[58, 59] The electrodes were fabricated with a thickness of 95 nm of Pt above 10 nm Cr plated onto 25×76×1 mm glass microscope slide (AmScope.com). Photolithography was utilized to create a master wafer from which polydimethylsiloxane (PDMS) castings were obtained for the fluidics. Electrodes were then overlaid by the PDMS circular microfluidic chamber.[58] The circular microfluidic chamber had a diameter and depth of 590 µm and ~70 µm, respectively. Disposable biopsy punches (Robbins Instruments, Chatham, NJ, USA) were utilized to create inlet and outlet ports of 300 µm in diameters.

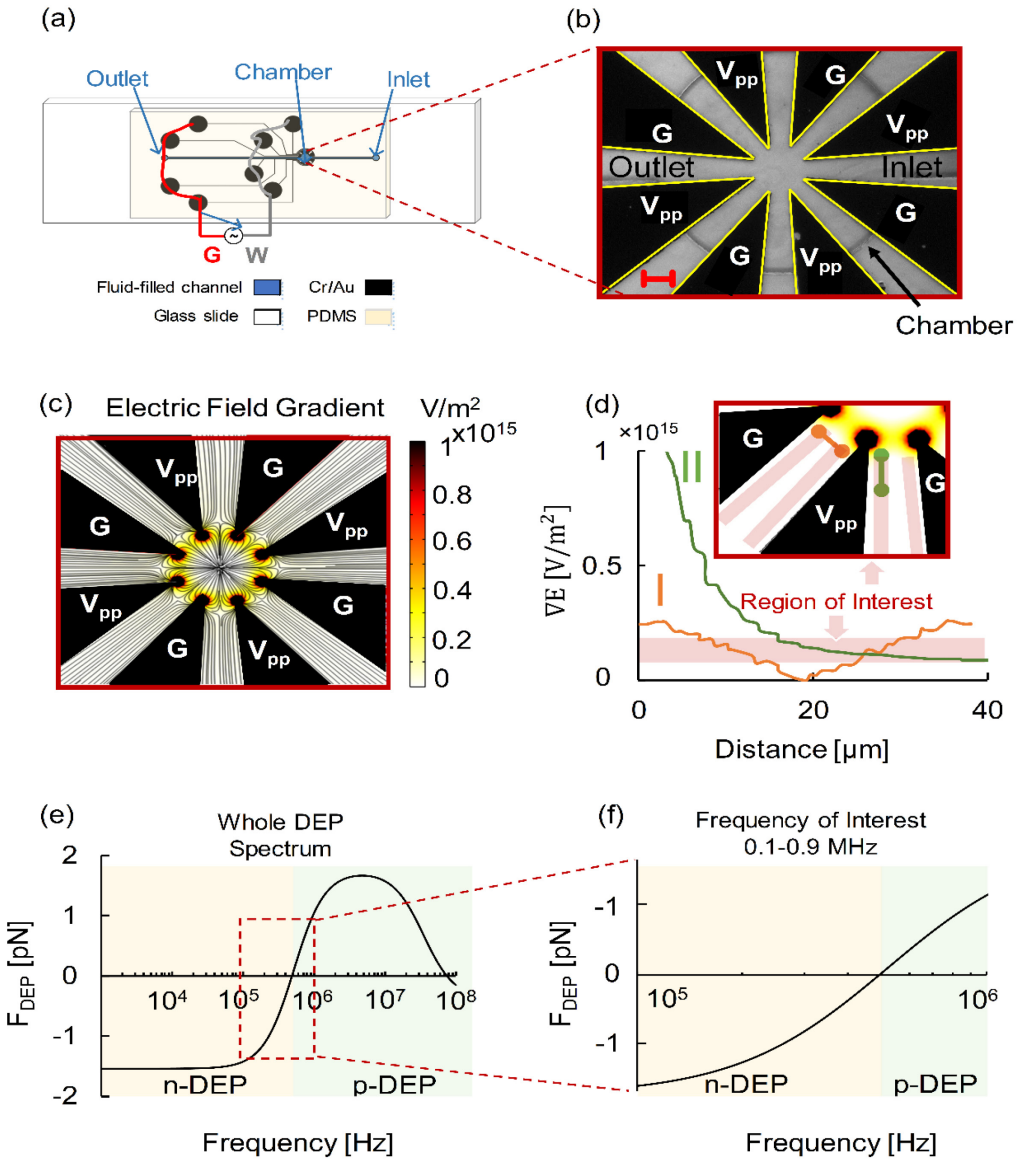

281

282 **Figure 1.** (a) Microfluidic device configuration with a PDMS fluidic layer bonded on a
283 microfabricated Cr/Au electrode glass slide. (b) Microscope image of the eight-electrode design
284 overlaid by a circular (d=590 µm) microfluidic chamber. The red scale bar is 50 µm. (c) Electric
285 field gradient (V/m^2) simulated using COMSOL Multiphysics® in 0.1 S/m medium at 0.1 V_{pp}/µm.
286 (d) Cutline of the electric field gradient parallel to electrodes (see inset) is shown in green (II),
287 while the electric field gradient perpendicular to the working and ground electrode (inset) is shown
288 in orange (I). (e) The generic spherical single-shell model predicts a low 0.45 MHz crossover
289 frequency for cells in 0.1 S/m medium. (f) Frequency range of interest for membrane polarizations.

DEP experiments

Samples (resuspended cells in iPBS) were introduced via an inlet port into the microfluidic chamber. The dielectrophoretic microfluidic device was then mounted on a Zeiss Axiovert microscope (Zeiss, Oberkochen, Germany). An AC potential was applied via a custom-built function generator (MicroDevice Engineering Inc., Houghton, MI, USA). Experiments were conducted at 5 V_{pp} with decreasing frequency from 0.9 to 0.1 MHz at a rate of 2400 Hz/s. According to Eq. (1), the electric field strength was calculated based on the external applied voltage (5 V_{pp}) over the shortest gap (50 μm) and used to compute the dielectrophoretic force. Cell movement was recorded via 10X video microscopy at 1 fpm for 343 seconds. Experiments were performed $n \geq 3$ (n = number of independent culture replicates) over 10 hours of observation at 0, 1.5, 4, 8, and 10 hours. Three repeats ($r \geq 3$) were conducted for each culture and time. In order to accurately record the DEP response, it is of great importance to minimize the cell population variation. Cell lysis significantly increases beyond 10 h post-PPV infection.[28] Video analysis in this work also revealed that PPV-infected cells experienced minor lysis at 10 hpi. Thus, to avoid variation in the cell population, DEP tests were performed up to 10 hours, but not longer. Cell populations were ~30 cells per experiment. Thus, a population of 270 cells was examined per time point with 3 replicates with independent cultures and 3 repeats with each culture. Since there are 5-time points (0, 1.5, 4, 8, and 10 hours), the data reported herein is roughly 1,350 cells.

Cell selection, data acquisition and analysis

As shown in Figure 1, the electric field in the eight electrode microdevice is non-uniform. This electric field non-uniformity induces motion in polarizable cells. Cells located in black, red, and dark orange regions in Figure 1b experience a greater DEP force than cells in light orange, yellow, and white regions. To ensure comparisons only reflected cell properties and not spatial field

properties, cells were selected within spatial field regions where equal force would be exerted on the cells. Cells were selected that fell within the similar electric field gradient shown in Figure 1c then tracked to accurately and reproducibly quantify displacement to determine cell velocity and subsequently DEP response. Non-infected (control), PPV-infected, glycine-treated/non-infected (glycine control), and glycine-treated/PPV-infected PK-13 cell DEP behaviors were quantified with Tracker 4.11.0 software (https://physlets.org/tracker/) to calculate the cell velocity. Using Eq. (3), the dielectrophoretic force ($\vec{F}_{DEP}$) was calculated and plotted. Statistical quartile analysis was performed on all data collected as a function of frequency. This was completed to generate a DEP force plot with five distinctive characteristics: minimum, first quartile, median, third quartile, and maximum. The median is the midpoint of the DEP force (comparable to averages utilized for traditional DEP spectra) while the first and third quartiles represent the middle 50% of the data. The traditional discrete box-and-whisker plot[60] was extended into a continuous box-and-whisker-inspired plot to display all data collected from the 1,350 cells tested.

Cell dielectrophoretic responses, R_c, were analyzed before and after glycine treatment at 0, 1.5, 4, 8, and 10 hours. The cell's dielectrophoretic responses were categorized into three subpopulation groups: n-DEP, p-DEP, p- to n-DEP. R_c (%) was calculated by dividing the number of cells in each group, n_i, exhibiting n-DEP or p-DEP (where $i =$ n-DEP, p-DEP, p- to n-DEP) by the total number of cells, n_T:[36]

$$R_c(\%) = \frac{n_i}{n_T} \times 100 \quad (5)$$

Cell optical contrast and morphology was observed to be indicative of the cell's transition from healthy to dead. Thus, ImageJ® software (NIH, https://imagej.nih.gov/ij/) was used to measure cell intensity within each video frame. Briefly, the intensity density of each cell, I, was normalized with respect to the maximum intensity density of the cell population, I_m. Histogram

graphs were utilized to plot the cell's dielectrophoretic response (R_c) versus the normalized intensity $\bar{I}$.

$$\bar{I} = \frac{I}{I_m} \quad (6)$$

Morphology was also measured and recorded with ImageJ® software. Cell size was obtained by capturing 2D microscopy images of ~30 cells per replicate and measuring the cell diameter using ImageJ®. Trends with PPV infection were examined from this data.

Calculation of dielectric properties

The C_{mem} was calculated via (i) first crossover frequency Eq. (4), and (ii) the spherical single-shell model fit to the DEP force spectra from 0.1 to 0.9 MHz. In the later method, the experimental $\vec{F}_{DEP}$ was compared to the theoretical $\vec{F}_{DEP}$ via mean absolute percentage error (MAPE) through an optimization algorithm in MATLAB. An average value of experimental $\vec{F}_{DEP}$ was used calculate the MAPE.[61]

Results and Discussion

This study examined the state and progression over time of PPV infection of PK-13 cells as well as the efficacy of a promising antiviral compound glycine using cell property quantification techniques. Membrane dielectric properties of PK-13 cells were calculated to elucidate membrane-related mechanisms during the progression of the PPV infection in the absence and presence of the osmolyte glycine.

Qualitative dielectrophoretic behavior

To piece together DEP response spectra, frequency sweeping measurements were explored from 0.1 to 0.9 MHz. The frequency sweep was conducted from high to low frequency because

the forces cells experience while undergoing p-DEP at higher frequencies are larger in magnitude than those forces cells experience when trapped at electric field minima while experiencing n-DEP; by sweeping from high to low, the p-DEP to n-DEP transition with f_{CO} was more reproducible. Figure 2 shows images extracted from the video of PK-13 cell DEP responses with the electric field off and at 0.8, 0.3, and 0.1 MHz (columns); field strength was fixed to 0.1 V_{pp}/µm in 0.1 S/m iPBS medium. Prior to applying the potential, non-infected PK-13 cells (control) were uniformly distributed in the chamber. After applying the signal, the majority of the non-infected PK-13 cell population was pushed toward the high electric field density regions, indicating p-DEP. Non-infected PK-13 cells exhibited mainly p-DEP from 0.9 MHz down to ~0.48-0.46 MHz. The cells then experienced a directional shift in force through the crossover frequency to then push the PK-13 cells towards the electric field minima between the electrodes and the chamber center.

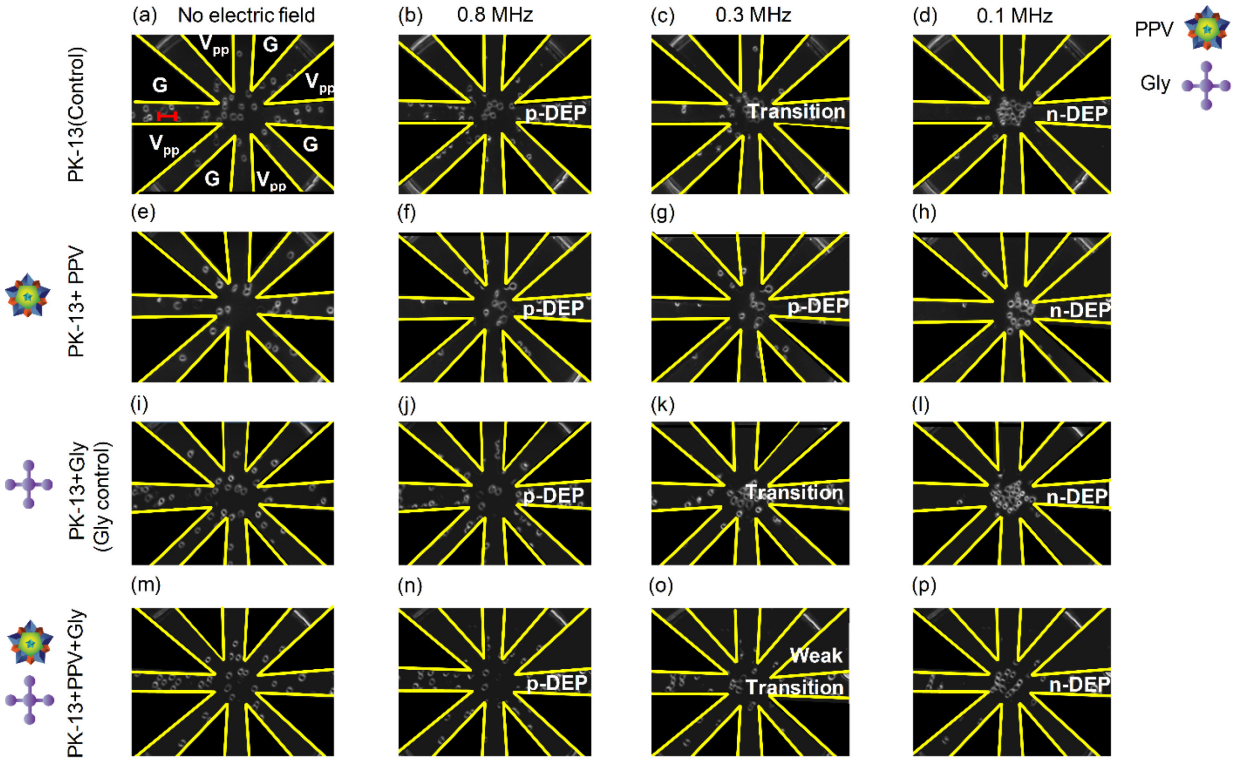

Figure 2. Experimental time sequence of PK-13 cells in 0.1 S/m iPBS at 0.1 V_{pp}/μm at specific frequencies during the frequency sweep. Data shown were 10 hours after infection and/or glycine addition. Images are shown at 0 sec and no electric field (a, e, i, and m), 42 sec corresponding to 0.8 MHz (b, f, j, and n), 250 sec corresponding to 0.3 MHz (c, g, k, and o), and 334 sec corresponding to 0.1 MHz (d, h, l, and p). Positive DEP and negative DEP are noted along with the directional transition. Scale bar in (a) is 50 μm.

In the second row of Figure 2, the 10-hour PPV-infected PK-13 cells also first experience p-DEP, but then crossover to n-DEP behavior occurred below ~0.3 MHz. Glycine-treated/non-infected PK-13 cells (glycine control, third row) showed behavior similar to non-infected PK-13 cells (control, first row). For glycine-treated/PPV-infected cells shown in the fourth row, a lethargic transition to n-DEP was observed below ~0.3 MHz. In summary, the DEP time-dependent videos revealed significant changes in crossover frequency and cell's dielectric properties at 10 hours after infection and glycine treatment.

The DEP behavior exhibited by PK-13 cells exposed to inactivated PPV did not change over 10 hours of observation [data not shown]. The fact that dielectric properties of PK-13 did not change to any significant extent in the presence of inactivated PPV strongly suggests that inactivated virus does not interact with the host cells. Thus, subsequent discussions focus on the PPV infection progression of PK-13 cells as well as antiviral efficacy of glycine.

Cell population analysis

The dielectrophoretic behavior of the entire cell population was divided into three subpopulation groups: n-DEP, p- to n-DEP, and p-DEP. A cell grouping methodology was employed because cells in the population did not all behave identically. High titers were used to infect the cell populations to have as many cells as possible infected at a multiplicity of infection (MOI) of 10 and to synchronize the infection cycle. Data on cell population data was collected from $n \geq 3$ replicates and $r \geq 3$ repeats. Variation between replicates and repeats were found to be

insignificant; thus, all data was combined into ensemble cell population dielectrophoretic responses and normalized intensity density. Figure 3a and c illustrate the stacked column representation of the cell population's dielectrophoretic responses, R_c (%), for PPV-infected/PK-13 cells before and after glycine treatment.[62] Cells that exhibit n-DEP over the whole frequency range were grouped as n-DEP (yellow color in Figure 3). The cell group with both p-DEP and n-DEP responses were clearly observable and classified as p- to n-DEP (grey color in Figure 3). Finally, blue was used to identify cells, only showing p-DEP over the entire frequency range. Upon applying the potential, most of the cell population (~>80%, grey and blue) experienced p-DEP. These cells showed brighter intensity than the background with well-defined rounded structures. Some cells (~<20%, yellow areas) were pushed toward the low electric field density region between the electrodes at the chamber center, showing n-DEP. These cells were not as bright as the grey and blue groups, and some contained visibly deformed membrane morphology.

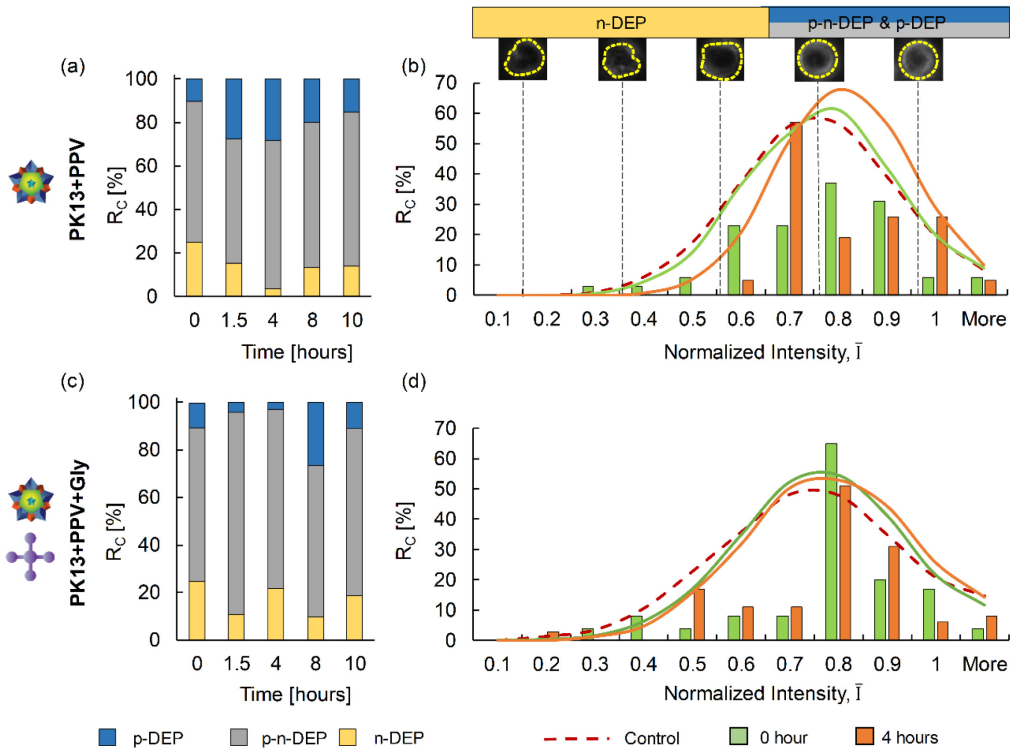

407

408 **Figure 3.** Cell's dielectrophoretic responses, R_c (%), stacked into a column chart for PPV-infected
409 PK-13 cells (a) without and (c) with glycine treatment from 0 to 10 hours. Cells that exhibit n-
410 DEP over the whole frequency range were grouped as yellow while p-DEP cells are shown in blue.
411 The notation p-n DEP indicates cells that initially exhibit p-DEP and then transitioned to n-DEP
412 (grey color). The histogram plot of cell's dielectrophoretic responses (R_c) versus normalized
413 intensity density for PK-13 cells and PPV-infected PK-13 cells without (b) and (d) with glycine
414 treatment at 0 and 4 hours.

415 Normalized intensity density, Ī, was utilized to quantify cellular brightness within each
416 subpopulation. Ī ranged from 0.2 as the lowest intensity with the darkest cell contrast to 1 as the
417 highest intensity with the brightest cell contrast. Figure 3b insets show the optical images of
418 representative PK-13 cells from the darkest (Ī=0.2) to the brightest (Ī=1) contrast within one
419 experimental run. Figure 3b and d show the histogram plot of cell dielectrophoretic responses, R_c
420 (%), versus normalized intensity, Ī, for non-infected (control), and PPV-infected PK-13 cells at 0
421 and 4 hours. The normalized intensity of non-infected PK-13 cells (control) was 0.70 ± 0.15. Upon

422 infection, $\bar{I}$ was 0.71 ± 0.15 at 0 hours and then shifted to 0.76 ± 0.13 at 4 hours. In the presence
423 of glycine, $\bar{I}$ of non-infected PK-13 cells (glycine control) was 0.73 ± 0.13. For glycine-
424 treated/PPV-infected cells, $\bar{I}$ was initially 0.73 ± 0.12 and shifted to 0.75 ± 0.16 at 4 hours. When
425 taken as a whole, there were not significant differences in $\bar{I}$. However, there were significant $\bar{I}$
426 differences between the subpopulation showing n-DEP over the frequency range of interest and
427 the other two subpopulation groups, p- to n-DEP and p-DEP. The results show that the n-DEP
428 subpopulation exhibits $\bar{I} \leq 0.6$ while subpopulations of p- to n-DEP and p-DEP have $\bar{I} \geq 0.6$. As
429 shown in Figure 3b, physical membrane irregularities such as shape and contrast were confined to
430 the $\bar{I} \leq 0.6$ subpopulation. This result indicates that DEP responses and measures are consistent
431 with traditional tools of optical examination of cell morphology, intensity, and contrast. As shown
432 in Figure 3a and c, the majority of the cells belong to the p- to n-DEP subpopulation. No significant
433 intensity or morphological differences were observed between p- to n-DEP and p-DEP groups.
434 Cells that exhibited p-DEP over the whole frequency range were likely experiencing mechanical
435 adhesion to the electrodes. Cell sticking is a common problem in microfluidic devices and our
436 previous work illustrated that surfactants could alter apparent cell dielectric properties.[38] Thus,
437 we chose to avoid the use of surfactants and simply disregard adhered cells.

438 To compile the DEP spectra in Figure 5, only cells experiencing both p-DEP and n-DEP were
439 utilized to measure velocity over the frequency range of interest. To provide further insight into
440 the two population behaviors (i.e., p- to n-DEP and n-DEP), a separate cell viability test was
441 performed to ascertain the ratio of viable and dead cells present in the cell suspension.

Cell membrane integrity

To ascertain subpopulations based on cell viability, cell membrane integrity was monitored by their ability to exclude trypan blue dye;[63] trypan blue tests were performed in the absence of an electric field. PK-13 cells were treated with trypan blue before and after glycine treatment for both non-infected and PPV-infected cells at incubation time points t = 0, 1.5, 4, 8, and 10 hours. Figure 4 shows trypan blue images for the non-infected (control) and PPV-infected PK-13 at t=10 hours.

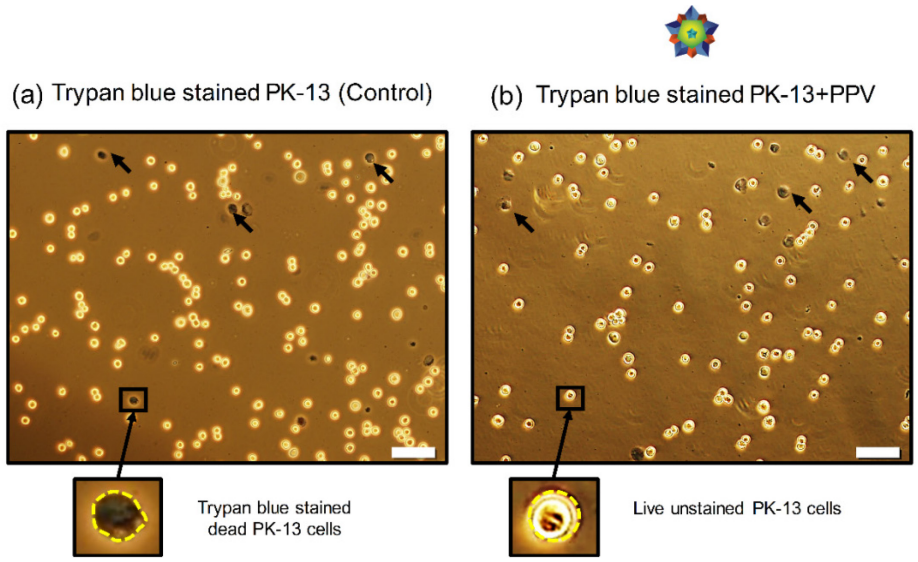

Figure 4. Trypan blue staining of PK-13 cells (a) before and (b) after PPV infection at t=10 hours. The dark blue stained cells delineated with black arrows represent dead cells while the bright centered cells are considered live. White scale bar is 20 μm.

A break in the integrity of the membrane immediately compromises the barrier functionality, thus killing the cell. Two main mechanisms leading to cell death are necrosis and apoptosis.[64] Previous research has documented that parvovirus infection usually induces apoptosis.[65] Apoptotic cells at earlier infection cycle stages exclude trypan blue, whereas late apoptosis or necrotic cells are quickly stained with trypan blue due to their extensive membrane damage. Zhang et al. showed that PPV infection induces apoptosis after 48 hours in PK-15 cells through activation of p53 via a mitochondria-mediated pathway.[65] Tafur et al. determined that infectious PPV virus began to

appear extracellularly after 15 hours and intracellularly after 10 hours without glycine addition.[28] This study explored the first 10 hours of the infection cycle during which the osmolyte anti-viral functionality occurred, and cell deaths were comparable to controls.

As shown in Figure 4a, dark cells delineated with black arrows represent dead trypan blue positive-stained cells that experienced necrotic or apoptotic cell death. These cells had visibly deformed membranes. Bright centered cells were alive, comprised a majority of cells in the culture, and had well-defined round structures. For untreated cell and cells earlier in the infection cycle, changes in viability for a small portion of the cell population are expected due to non-infection influences such as cell physiology,[66] chemical abnormalities,[67] medium pH and tonicity,[68] mechanical forces,[69] and temperature changes.[70] Comparison of stained and unstained cells with both color and greyscale microscopy revealed that dead cells from the same sample had membrane irregularities and displayed the darkest cell contrast ($\bar{I} \leq 0.6$); interestingly, dark contrast cells exhibited n-DEP over the whole frequency range as shown in Figure 3. As a representative example, the relative abundance for n-DEP was 14% for PPV infection at 10 hpi, which was comparable to the 13% trypan blue stained dead PK-13 cells at 10 hpi (Figure 4a and b). Data was ensembled together to conduct a t-test; no significant difference (p-value < 0.05) was found between the population of n-DEP (Figure 3a and c) and that of the trypan blue stained dead PK-13 cells. Thus, it was concluded that n-DEP behavior was an indicator for dead cells. This suggests dead cells experience n-DEP and their exclusion from further analysis is justified.

Quantitative dielectrophoretic spectra

Velocities were measured from videos of PK-13 cell DEP responses to frequency sweeps from 0.9 MHz down to 0.1 MHz.[36, 71] Cell velocities were compiled, converted to force via Eq. (3) and then used to assemble PK-13 DEP response spectra for cells experiencing both p-DEP and n-

DEP (Figure 5). Time-dependent changes in the DEP response spectra of cells were tracked after infection for both untreated and glycine-treated PPV-infected PK-13 cell populations at incubation time points t = 0, 1.5, 4, 8, and 10 hours.

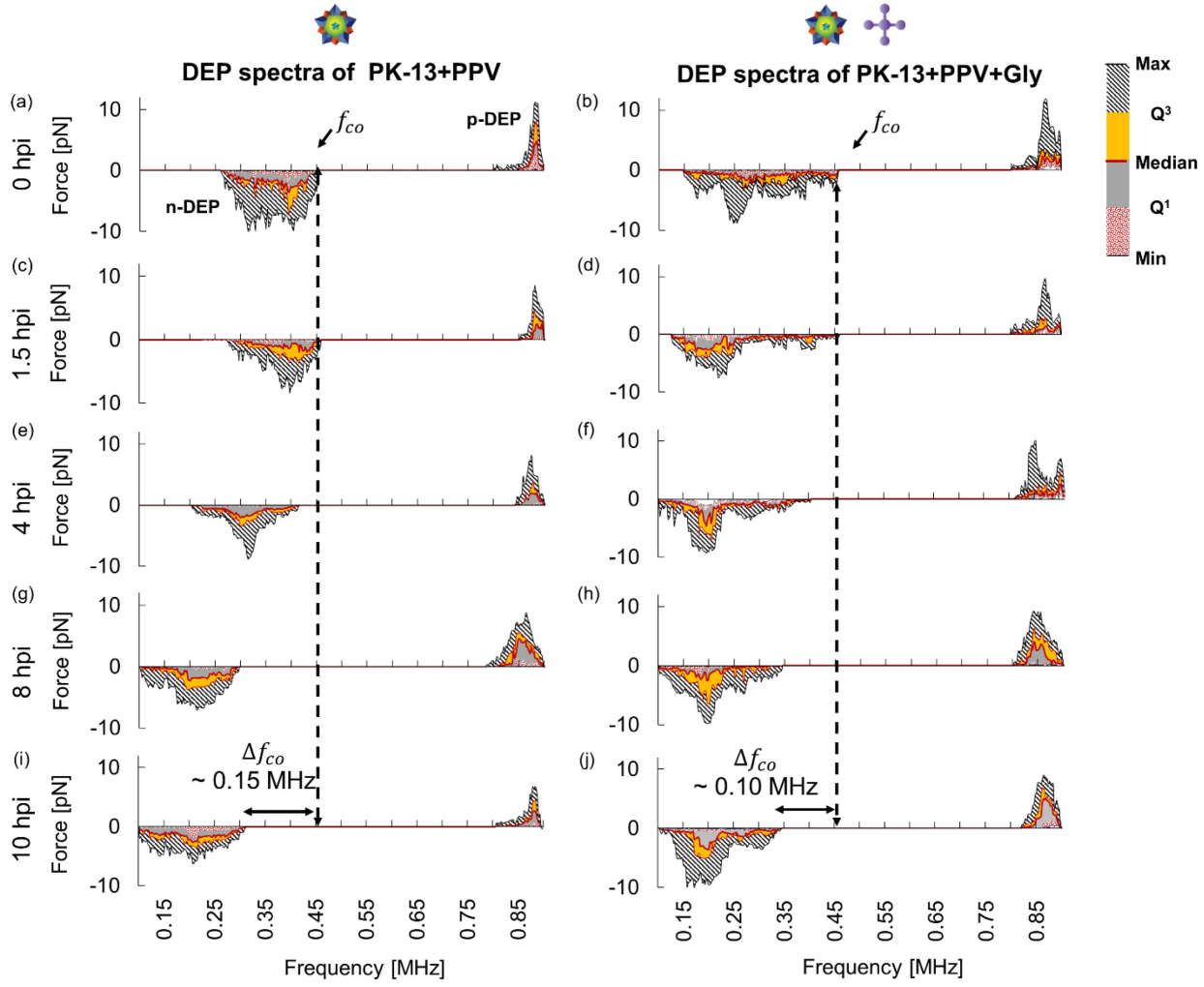

Figure 5. Dielectrophoretic force spectra of untreated (first column) and glycine-treated (second column) PK-13 cells post infection as function of frequency 0.9 to 0.1 MHz at (a and b) 0 hours, (c and d) 1.5 hours, (e and f) 4 hours, (g and h) 8 hours, and (i and j) 10 hours. PK-13 cell velocities were utilized to calculate DEP forces at each frequency. The resulting DEP force profiles are shown via a box-and-whisker-inspired representation of all cells measured. The dotted red, grey, yellow, and hashed grey colored regions show the first, second (aka median), third, and fourth interquartile ranges, respectively while the min and max solid lines for the whiskers show the full force range (patterned area) for all cells in the equivalent electric field test region.

Figure 5 uses a continuous box-and-whisker- inspired representation whereby the dotted red, grey, yellow, and hashed grey colored regions show the first, second (aka median), third, and fourth

interquartile ranges, while the black solid lines for the whiskers show the full force range demonstrated by cells. This representation is a concise tool to illustrate the motion of every cell in the equivalent electric field region of interest (Figure 1).[44] Each frequency's data represents 14 to 22 individual cells (n≥3 and r≥3).

Two controls were conducted. Insignificant differences were observed between the DEP spectra of non-infected PK-13 (control) and glycine-treated/non-infected PK-13 (glycine control) cells over 0, 1.5, 4, 8, and 10 hours. Both of the control and glycine control cell populations consistently yielded f_{CO} of 0.45 ± 0.02 MHz and 0.44 ± 0.01 MHz, respectively indicating the presence of glycine did not impact polarization characteristics of PK-13 cells.

Upon PPV infection, the DEP spectra and the f_{CO} remained unchanged for the first 1.5 hours. However, after 4 hours, the infected cells' f_{CO} decrease from 0.45 ± 0.02 MHz to 0.38 ± 0.02 MHz. Previous studies showed that virus capsids and then the newly formed infectious virus were only discernable intracellularly after 8 and 10 hours, respectively.[27, 28] The shifting of the DEP spectra after 4 hours as shown in Figure 5 suggests that earlier stages of infection were discernable via dielectrophoretic responses. These earlier stages of infection presumably involve virus binding to the cell membrane, formation of clathrin-coated pits in the membrane and then endocytic transport across the membrane into the cell.[27, 28] At 8 and 10 hours, the infected PK-13 DEP spectra shifted even lower yielding f_{CO} of 0.26 ± 0.02 MHz and 0.27 ± 0.01 MHz, respectively. It should be noted that viral entry can continuously occur during the course of PPV exposure to PK-13 cells. Thus, PPV has an additional 4 to 6 hours for binding and internalization.

As shown in Figure 5a and b, for glycine-treated/PPV-infected cells, the f_{CO} of the DEP spectra were similar to that of PPV-infected cells for the first 4 hours. However, n-DEP behaviors extend from 0.45- 0.30 MHz and 0.44-0.15 MHz for non-infected PK-13 and glycine-treated/non-

519 infected PK-13, respectively. Similar n-DEP trends were observed up to 4 hpi. However, after 8
520 and 10 hours, the glycine-treated/PPV-infected cells displayed f_{CO} shifts down to only 0.33 ± 0.02
521 MHz at both 8 and10 hours, which was an attenuated response compared to the PPV infected cells
522 without glycine. Thus, glycine slightly alters the DEP force spectra of the first four hours of the
523 initial infection cycle that is indicative of the virus entry process and significantly attenuated viral
524 effects discernable with the DEP spectra shift - at 8 and 10 hours. These results suggest that glycine
525 did not impede virus penetration into the cell, but it did alter the interfacial field-induced charge
526 distribution over time manifesting as a difference in the DEP f_{CO} and spectra patterns.

527 **Virus capsid protein production with the addition of glycine**

528 Tafur et al. showed the PPV infectivity reduction in the presence of glycine by quantifying
529 the extent of virus capsid protein formation within the PK-13 cells using immunostaining of the
530 PPV capsid proteins and DAPI staining of the viral nucleus (DAPI concentration 150 μM). DAPI
531 is a nucleic acid stain for DNA and is impermeable to live cells at low concentration, allowing it
532 to discriminate intact from membrane-compromised cells.[72] Figure 6 shows the ratio of PPV capsid
533 proteins to DAPI from 0 to 12 hours in order to normalize the amount of PPV capsid proteins per
534 cell. No capsid proteins were detected in the PBS negative control. PPV capsid proteins were
535 found in both untreated and glycine-treated PPV-infected cells. The fluorescence ratio of PPV
536 capsid proteins to the count of DAPI increased by 8 hours after infection. Thus, virus capsid
537 proteins appear intracellularly 8 hours after infection, which agrees with virus production data,[28]
538 and DNA production data.[27]

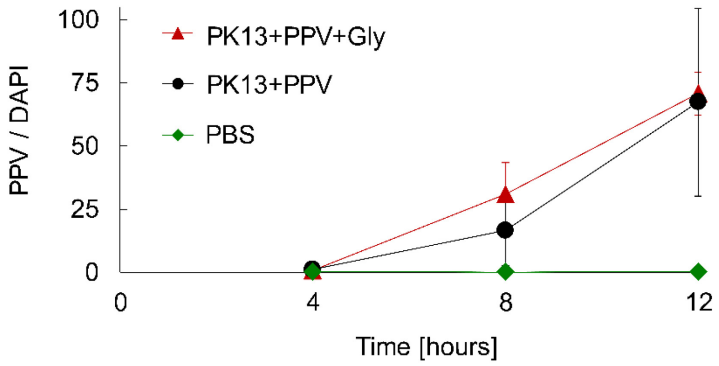

Figure 6. The impact of osmolytes on virus capsid protein formation is captured via the ratio of PPV capsid proteins to the fluorescent DAPI count. All data points are the average of three independent samples with 10 images per sample, and the error bars represent the standard deviation. Data obtained in concert with Tafur et al. data acquisition.[28]

Infected cells decrease f_{CO} by only ~15% within 4 hours of infection; this is consistent for both the absence and presence of glycine (Figure 5). By 10 hours, the PPV-infected cells shifted f_{CO} by ~42% while f_{CO} of glycine-treated PPV-infected cells shifted down by ~25%. In short, the presence of glycine did not completely prevent the DEP spectra shift toward lower frequencies. These results suggest that viral infection as well as the antiviral effects of high intracellular concentrations of glycine that are likely associated with virus capsid proteins, impact interfacial field-induced charge distributions that are discernable dielectrophoretically. Additionally, cytoplasm homeostasis would be altered due to (i) the formation of capsid/new virus, and (ii) the presence of glycine. In the following section, the values for specific membrane capacitance were calculated using the crossover frequency and spherical single-shell model.

Cell membrane capacitance

The cell's transition from a healthy to a diseased state is often associated with changes in the dielectric properties of the cell (i.e. specific membrane capacitance, C_{mem}).[12-17, 20-24] The C_{mem} can be used as an electrophysiological marker to diagnose disease, track disease progression, and help vet treatment strategies for tailored disease management. As shown in Eq. (4), the C_{mem} is a

559 function of crossover frequency (f_{CO}), medium conductivity (σ_m), and cell radii (r). Medium
560 conductivity, σ_m, strongly affects the cell behavior in the β-dispersion region.[10] Thus, in our
561 experiments and in our DEP model, σ_m is kept constant at 0.1 S/m. As shown previously (Figure
562 5), the crossover frequency was determined experimentally and quantified from DEP force data.
563 Additionally, this DEP spectra from 0.1 to 0.9 MHz was fit to a spherical single-shell model to (i)
564 calculate C_{mem}, and (ii) further evaluate the calculated specific cell membrane capacitance via f_{CO}.
565 Agreement between the crossover frequency and curve-fitting methods was highly consistent
566 (difference of ~3%). Values from the DEP spectral fit are reported in all subsequent discussions.
567 To more accurately calculate C_{mem}, the impact of cell radius was also studied.
568 Maxwell-Wagner interfacial polarizations govern cell responses in the β-dispersion region
569 whereby the magnitude of the interfacial polarization rises with increasing radius of a cell.[7, 47] Eq.
570 (1) and Eq. (3) explain how cell radius impacts DEP force magnitude and f_{CO}, respectively. Figure
571 7a and c are the box-and-whisker-plots of cell radii for non-infected (controls) and PPV-infected
572 PK-13 cells before and after glycine treatment at t = 0, 1.5, 4, 8, and 10 hours. The box-and-
573 whisker-plots illustrate the distribution of radii based on the median, second quartile (grey), third
574 quartile (yellow), and range (minimum and maximum values). The mean and standard deviation
575 were utilized to develop a statistical representation of cell radius.
576

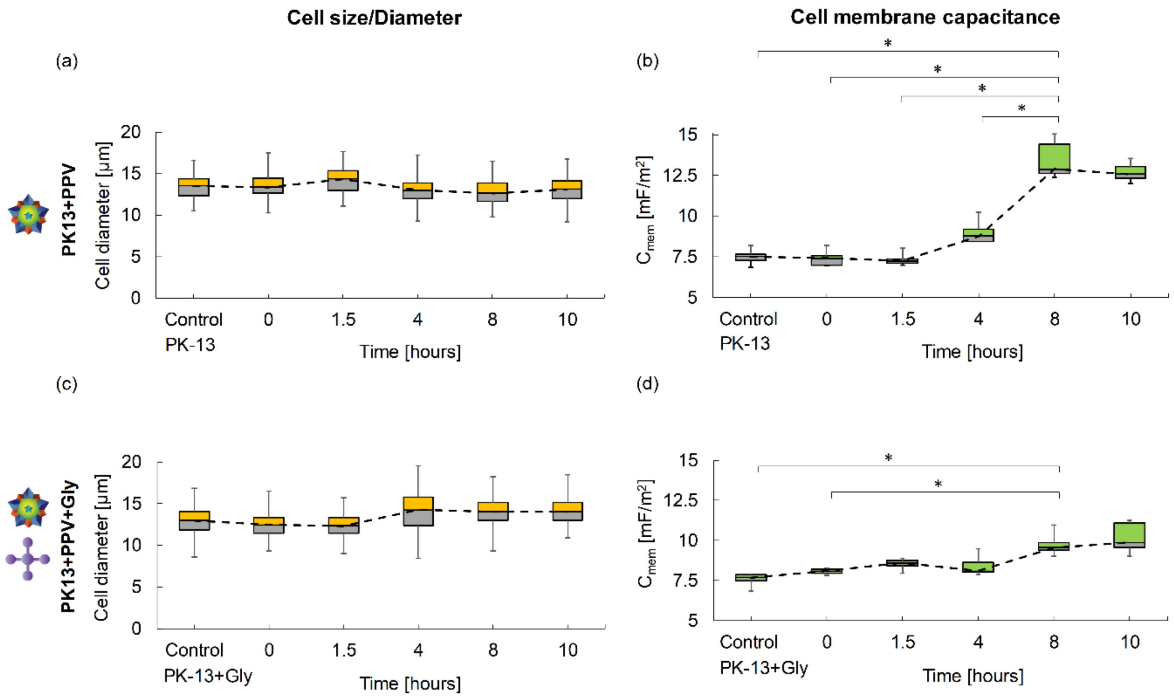

577

578 **Figure 7.** Box-and-whisker-plots of cell radii for non-infected (controls) and PPV-infected cells (a) without
579 and (c) with glycine treatment. Cell radii of PPV-infected and glycine treated/PPV-infected cells are shown
580 at t = 0, 1.5, 4, 8, and 10 hours. Plots illustrate the size distribution with the median, second quartile (grey),
581 third quartile (yellow), and range (minimum and maximum values). Cell membrane capacitance of non-
582 infected (controls) and PPV-infected cells (b) without and (d) with glycine treatment. The second quartile
583 and third quartile are shown in grey and green color, respectively. * represents p-value <0.05.

584 Cell radii of non-infected PK-13 cells (control) were 6.67 ± 0.70 µm. Upon infection, the cell
585 radius was 6.76 ± 0.73 and 6.54 ± 0.75 µm at 0 and 10 hours, respectively. The observed difference
586 in cell radii is not statistically significant. In the presence of glycine, the cell radii of non-infected
587 PK-13 cells (glycine control) was slightly smaller at 6.45 ± 0.83 µm. The radii of glycine-
588 treated/PPV-infected cells were 6.22 ± 0.81 and 7.12 ± 0.88 µm at 0 and 10 hours, respectively.
589 These radii changes were minimally statistically different (p-value=0.86). The observed slight
590 increase in cell diameter after glycine treatment can be explained by the accumulation of
591 unassembled capsid protein inside the cell. Cell radius variation was found to be insufficient to
592 explain the DEP spectra alterations at 10 hpi (Figure 7).

Figure 7b and d are the box-and-whisker-plots of cell membrane capacitance calculated via Eq. (4) for non-infected (controls) and PPV-infected PK-13 cells without and with glycine treatment at t = 0, 1.5, 4, 8, and 10 hours. The second and third quartiles are shown in grey and green colors, respectively. The cell membrane capacitance of non-infected PK-13 cells (control) was found to be 7.4 ± 0.4 mF/m^2. With infection, the cell membrane capacitance was initially similar to the non-infected PK-13 cells (control). The cell membrane capacitance began to increase after 4 hours, suggesting that infection induced PK-13 cells can be identified as early as 4 hpi. The membrane capacitance of PPV-infected cells increased to 13.3 ± 1.0 mF/m^2 after 8 hours and settled to 12.7 ± 0.4 mF/m^2 at 10 hours. The statistical analysis, shown in Figure 7b, revealed significant differences between the cell membrane capacitance of the PPV-infected cells at t = 0, 1.5, and 4 compared to the cells at t=8 and 10 hours (*, p-value <0.05). The results show that C_{mem} increased by more than 70% over the 10 hours. The membrane capacitance reflects charge imbalances during virus membrane infusion, viral component synthesis, and assembly of progeny virus. Similar observations have been reported for other cell lines and viruses.[23, 24] Membrane conductance was calculated to be 10^{-6} S/m and did not change significantly during the course of PPV exposure to PK-13 cells in the absence and presence of glycine. Typically, increases in membrane conductance and ion leakage occur at late-stage cell death,[48] which for PK-13 occurs at times longer than 10 or 12 hours.

Previous studies have shown that characteristic capacitance and cell dielectric properties are correlated in viral infection cycles.[22-24] Both increases and decreases in the membrane capacitance have been reported. Differences in characteristic capacitance and cell dielectric properties appear to be specific to the type of virus (enveloped/non-enveloped), viral size, intracellular location of viral protein/capsid assembly, and cell line/size.[24] Variations in C_{mem} could also be brought about

by changes in membrane thickness and dielectric composition as the cell responds to viral penetration. In broader cell studies, different trends appear to be associated with membrane composition and membrane folding.[22-24] Higher values of membrane capacitance indicate more blebs, folds, ruffles, and microvilli in the cell membrane while lower values demonstrate the loss of microvilli and membrane smoothing.[7]

To the best of our knowledge, no previous DEP studies have identified a means to reverse or impede viral impacts on a cell population using a natural antiviral compound. Immediately upon glycine treatment, non-infected PK-13 cells had a membrane capacitance of 7.5 ± 0.2 mF/m^2. The cell membrane capacitance increased to 8.4 ± 0.6 mF/m^2 after 4 hours and then up to 9.8 ± 0.6 mF/m^2 and 10.1 ± 1.1 mF/m^2 at 8 and 10 hours, respectively. Membrane capacitance values with glycine increased by 34.7% over the 10 hours. In comparing Figure 7b and d, the most significant differences were observed at t= 8 and 10 hours whereby the membrane capacitance was 26.3% and 20.5% lower, respectively, for glycine-treated/PPV-infected cells than for untreated cells. The markedly reduced membrane capacitance following glycine therapy suggests that high intra and extracellular concentrations of this osmolyte can significantly halt charge imbalances across the infected membrane. The markedly reduced membrane capacitance following glycine therapy suggests that the drug reduces the complexity of the membrane topography as the infection progresses.

In summary, the optical microscopy, intensity analysis, stain test, and β-dispersion region DEP were utilized to examine 10-hour trends for non-infected, PPV-infected, glycine-treated/non-infected, and glycine-treated/PPV-infected PK-13 cells. The increased C_{mem} of PK-13 cells over 10 hours altered DEP spectra and decreased f_{CO}. This trend was much less apparent in the presence

638 of glycine. Here, we demonstrated DEP potential to passively monitor membrane-related
639 mechanisms during a viral infection in the absence and presence of an antiviral compound.

640 **Conclusions**

641 In this study, DEP polarization mechanisms were studied during cell transitions from a healthy
642 to an infected state in the absence and presence of a promising antiviral compound. This work
643 focused on membrane polarization properties (predominantly membrane capacitance) of PK-13
644 cells without and with PPV infection as well as without and with glycine at incubation time points
645 t = 0, 1.5, 4, 8, and 10 hpi. Traditional cell characterization techniques (i.e., optical and staining
646 examinations) were also employed to compare PK-13 cells' integrity and viability against DEP
647 characterizations.

648 The PK-13 cells did not all behave identically in the DEP microchamber. Thus, methodologies
649 were developed based on morphology, intensity, contrast, and trypan blue dye-exclusion to
650 accurately measure DEP spectra for subpopulations of PK-13. Non-infected PK-13 cell
651 populations consistently yielded DEP spectra with cross over frequencies, f_{CO}, of 0.45 ± 0.02 MHz
652 over the 10 hours. Upon PPV infection, the f_{CO} decreased to 0.27 ± 0.01 MHz at 10 hours. Previous
653 studies showed that virus attachment, penetration, and virus capsid assembly occurs from 1.5 to 4
654 hpi, while infectious PPV virus began to appear intracellularly around 10 hpi.[27, 28] With glycine
655 treatment, the DEP spectra displayed attenuated DEP spectra and f_{CO} shifts from 0.44 ± 0.01 MHz
656 down to 0.33 ± 0.02 MHz for the glycine-treated/non-infected and glycine-treated/PPV-infected
657 PK-13 cells, respectively. It is of interest to note that the n-DEP pattern of the DEP spectra alters
658 upon glycine treatment. However, the timing of DEP spectral shifts suggested that glycine anti-
659 viral mechanisms occurred post viral penetration into the cell.

660 To understand the underlying viral infection mechanisms, a spherical single-shell was utilized
661 to fit dielectric parameters to experimentally quantified DEP force data from 0.1 to 0.9 MHz for
662 the PK-13 cells. Each cell population was analyzed to ascertain any patterns of cell membrane
663 capacitance. With infection, C_{mem} increased by more than 70% over the 10 hours. This trend is
664 greater than for a non-enveloped reovirus where C_{mem} increased by 25% during viral infection.[24]
665 Glycine treatment lowered the elevated PK-13 cell membrane capacitance by 26.3% and 20.5% at
666 8 and 10 hpi, respectively. Our results are consistent with prior findings that glycine anti-viral
667 effects occur post cell infection. Since the PPV virus still penetrated the cell, DEP spectral shifts
668 were observed relative to the uninfected control. It should be noted that cell size did not change
669 significantly over the 10-hour infection cycle and thus DEP changes are attributed to membrane
670 properties, not cell size. However, the glycine-treated/PPV-infected PK-13 cells were slightly
671 larger in size, which can be attributed to the accumulation of the glycine and unassembled capsid
672 protein inside the cell.

673 Results showed that near real-time monitoring of cell membrane capacitance is an excellent
674 indicator of the cell's pathological state. The DEP results illustrated that significant changes in the
675 membrane capacitance and thus integrity could be identified earlier in the infection cycle than via
676 traditional viral staining and optical observations.

677 This work also illustrated a valuable application of cell population DEP for viral drug
678 screening. Results demonstrated that complexing DEP technology with pathology-based
679 observations increased the quantification and resolvability when monitoring the progression of
680 disease electrophysiological properties and therefore was powerful enough to vet therapeutic
681 treatment strategies. This work linked dielectric measurements with pathological observations,
682 and as a consequence, the knowledge gained has the potential to enable dielectric-only

683 measurements to infer cell pathological states. Future applications could extend into diagnoses of
684 viral diseases including the tracking of disease progression in response to anti-viral therapies.

685 **Acknowledgment**

686 The authors gratefully acknowledge funding for Sanaz Habibi from a graduate teaching
687 assistance-ship and a doctoral finishing fellowship from Michigan Technological University.
688 Supplemental funding for Sanaz Habibi and the development of the frequency sweep technique
689 was supported by National Science Foundation (NSF) IIP 1632678 and IIP 1417187. Funding
690 support for Pratik U. Joshi and Xue Mi came from NSF 1451959 and 1510006.

691 **References**

692 1. Minerick, A. R., The rapidly growing field of micro and nanotechnology to measure living cells.
693 *AIChE journal* **2008,** *54* (9), 2230-2237.
694 2. Yi, C.; Li, C.-W.; Ji, S.; Yang, M., Microfluidics technology for manipulation and analysis of
695 biological cells. *Analytica chimica acta* **2006,** *560* (1-2), 1-23.
696 3. Ohno, K.; Tachikawa, K.; Manz, A., Microfluidics: applications for analytical purposes in
697 chemistry and biochemistry. *Electrophoresis* **2008,** *29* (22), 4443-53.
698 4. Yang, J.; Huang, Y.; Wang, X.-B.; Becker, F. F.; Gascoyne, P. R., Differential analysis of human
699 leukocytes by dielectrophoretic field-flow-fractionation. *Biophysical journal* **2000,** *78* (5), 2680-2689.
700 5. Muller, T.; Pfennig, A.; Klein, P.; Gradl, G.; Jager, M.; Schnelle, T., The potential of
701 dielectrophoresis for single-cell experiments. *IEEE engineering in medicine and biology magazine* **2003,**
702 *22* (6), 51-61.
703 6. Gimsa, J.; Wachner, D., A unified resistor-capacitor model for impedance, dielectrophoresis,
704 electrorotation, and induced transmembrane potential. *Biophys J* **1998,** *75* (2), 1107-16.
705 7. Pethig, R. R., *Dielectrophoresis: Theory, methodology and biological applications*. John Wiley &
706 Sons: 2017.
707 8. Jones, T. B., *Electromechanics of particles*. Cambridge University Press: 2005.
708 9. Nieuwenhuis, J. H.; Vellekoop, M. J., Simulation study of dielectrophoretic particle sorters.
709 *Sensors and actuators B: Chemical* **2004,** *103* (1-2), 331-338.
710 10. Gascoyne, P.; Pethig, R.; Satayavivad, J.; Becker, F. F.; Ruchirawat, M., Dielectrophoretic
711 detection of changes in erythrocyte membranes following malarial infection. *Biochimica et Biophysica*
712 *Acta (BBA)-Biomembranes* **1997,** *1323* (2), 240-252.
713 11. Adams, T. N. G.; Leonard, K. M.; Minerick, A. R., Frequency sweep rate dependence on the
714 dielectrophoretic response of polystyrene beads and red blood cells. *Biomicrofluidics* **2013,** *7* (6), 64114-
715 64114.
716 12. Srivastava, S. K.; Daggolu, P. R.; Burgess, S. C.; Minerick, A. R., Dielectrophoretic
717 characterization of erythrocytes: positive ABO blood types. *Electrophoresis* **2008,** *29* (24), 5033-46.
718 13. Shafiee, H.; Sano, M. B.; Henslee, E. A.; Caldwell, J. L.; Davalos, R. V., Selective isolation of
719 live/dead cells using contactless dielectrophoresis (cDEP). *Lab on a chip* **2010,** *10* (4), 438-45.

14. Hsiung, L.-C.; Chiang, C.-L.; Wang, C.-H.; Huang, Y.-H.; Kuo, C.-T.; Cheng, J.-Y.; Lin, C.-H.; Wu, V.; Chou, H.-Y.; Jong, D.-S., Dielectrophoresis-based cellular microarray chip for anticancer drug screening in perfusion microenvironments. *Lab on a chip* **2011,** *11* (14), 2333-2342.
15. Mahabadi, S.; Hughes, M. P.; Labeed, F. H., Abstract 3490: Measurement of Gifinitib (ZD1839) effect on electrophysiological properties of head and neck cancer cells using Dielectrophoresis (DEP). *Cancer Research* **2014,** *74* (19 Supplement), 3490-3490.
16. Huang, C.; Liu, H.; Bander, N. H.; Kirby, B. J., Enrichment of prostate cancer cells from blood cells with a hybrid dielectrophoresis and immunocapture microfluidic system. *Biomedical microdevices* **2013,** *15* (6), 941-948.
17. Liang, X.; Graham, K. A.; Johannessen, A. C.; Costea, D. E.; Labeed, F. H., Human oral cancer cells with increasing tumorigenic abilities exhibit higher effective membrane capacitance. *Integrative biology : quantitative biosciences from nano to macro* **2014,** *6* (5), 545-54.
18. Su, Y.-H.; Warren, C. A.; Guerrant, R. L.; Swami, N. S., Dielectrophoretic monitoring and interstrain separation of intact Clostridium difficile based on their S (Surface)-layers. *Analytical chemistry* **2014,** *86* (21), 10855-10863.
19. Khoshmanesh, K.; Baratchi, S.; Tovar-Lopez, F. J.; Nahavandi, S.; Wlodkowic, D.; Mitchell, A.; Kalantar-zadeh, K., On-chip separation of Lactobacillus bacteria from yeasts using dielectrophoresis. *Microfluidics and Nanofluidics* **2012,** *12* (1), 597-606.
20. Gascoyne, P.; Satayavivad, J.; Ruchirawat, M., Microfluidic approaches to malaria detection. *Acta tropica* **2004,** *89* (3), 357-369.
21. Nascimento, E. M.; Nogueira, N.; Silva, T.; Braschler, T.; Demierre, N.; Renaud, P.; Oliva, A. G., Dielectrophoretic sorting on a microfabricated flow cytometer: Label free separation of Babesia bovis infected erythrocytes. *Bioelectrochemistry* **2008,** *73* (2), 123-128.
22. Archer, S.; Morgan, H.; Rixon, F. J., Electrorotation studies of baby hamster kidney fibroblasts infected with herpes simplex virus type 1. *Biophys J* **1999,** *76* (5), 2833-42.
23. Yafouz, B.; Kadri, N. A.; Rothan, H. A.; Yusof, R.; Ibrahim, F., Discriminating dengue-infected hepatic cells (WRL-68) using dielectrophoresis. *Electrophoresis* **2016,** *37* (3), 511-518.
24. Petiot, E.; Ansorge, S.; Rosa-Calatrava, M.; Kamen, A., Critical phases of viral production processes monitored by capacitance. *Journal of biotechnology* **2017,** *242*, 19-29.
25. Organization, W. H., World Health Organization Model List of Essential In Vitro Diagnostics First edition (2018). *Geneva: World Health Oraganization* **2018**.
26. Halder, S.; Ng, R.; Agbandje-McKenna, M., Parvoviruses: structure and infection. *Future Virology* **2012,** *7* (3), 253-278.
27. Boisvert, M.; Fernandes, S.; Tijssen, P., Multiple pathways involved in porcine parvovirus cellular entry and trafficking toward the nucleus. *Journal of virology* **2010,** *84* (15), 7782-7792.
28. Tafur, M. F.; Vijayaragavan, K. S.; Heldt, C. L., Reduction of porcine parvovirus infectivity in the presence of protecting osmolytes. *Antiviral research* **2013,** *99* (1), 27-33.
29. Prikhod'ko, G. G.; Reyes, H.; Vasilyeva, I.; Busby, T. F., Establishment of a porcine parvovirus (PPV) DNA standard and evaluation of a new LightCycler nested-PCR assay for detection of PPV. *Journal of virological methods* **2003,** *111* (1), 13-19.
30. Heegaard, E. D.; Brown, K. E., Human parvovirus B19. *Clinical microbiology reviews* **2002,** *15* (3), 485-505.
31. Tsai, B., Penetration of nonenveloped viruses into the cytoplasm. *Annu. Rev. Cell Dev. Biol.* **2007,** *23*, 23-43.
32. Farr, G. A.; Zhang, L.-g.; Tattersall, P., Parvoviral virions deploy a capsid-tethered lipolytic enzyme to breach the endosomal membrane during cell entry. *Proceedings of the National Academy of Sciences* **2005,** *102* (47), 17148-17153.

33. Mushtaq, S.; Abbasi, B. H.; Uzair, B.; Abbasi, R., Natural products as reservoirs of novel therapeutic agents. *EXCLI journal* **2018,** *17*, 420.
34. Kitazato, K.; Wang, Y.; Kobayashi, N., Viral infectious disease and natural products with antiviral activity. *Drug Discov Ther* **2007,** *1* (1), 14-22.
35. Bolen, D. W., Effects of naturally occurring osmolytes on protein stability and solubility: issues important in protein crystallization. *Methods* **2004,** *34* (3), 312-322.
36. Adams, T.; Leonard, K.; Minerick, A., Frequency sweep rate dependence on the dielectrophoretic response of polystyrene beads and red blood cells. *Biomicrofluidics* **2013,** *7* (6), 064114.
37. Minerick, A. R.; Collins, J. L.; Leonard, K. M.; Adams, T. N., Methods and systems for identifying a particle using dielectrophoresis. Google Patents: 2016.
38. Habibi, S.; Lee, H. Y.; Moncada-Hernandez, H.; Gooding, J.; Minerick, A. R., Impacts of low concentration surfactant on red blood cell dielectrophoretic responses. *Biomicrofluidics* **2019,** *13* (5), 054101.
39. Srivastava, S. K.; Artemiou, A.; Minerick, A. R., Direct current insulator-based dielectrophoretic characterization of erythrocytes: ABO-Rh human blood typing. *Electrophoresis* **2011,** *32* (18), 2530-2540.
40. Gagnon, Z. R., Cellular dielectrophoresis: applications to the characterization, manipulation, separation and patterning of cells. *Electrophoresis* **2011,** *32* (18), 2466-2487.
41. Demircan, Y.; Ozgur, E.; Kulah, H., Dielectrophoresis: applications and future outlook in point of care. *Electrophoresis* **2013,** *34* (7), 1008-27.
42. Pethig, R., Dielectrophoresis: Status of the theory, technology, and applications. *Biomicrofluidics* **2010,** *4* (2), 022811.
43. Arnold, W.; Zimmermann, U., Rotating-field-induced rotation and measurement of the membrane capacitance of single mesophyll cells of Avena sativa. *Zeitschrift für Naturforschung C* **1982,** *37* (10), 908-915.
44. Allen, D. J.; Accolla, R. P.; Williams, S. J., Isomotive dielectrophoresis for parallel analysis of individual particles. *Electrophoresis* **2017,** *38* (11), 1441-1449.
45. Pethig, R.; Kell, D. B., The passive electrical properties of biological systems: their significance in physiology, biophysics and biotechnology. *Physics in Medicine & Biology* **1987,** *32* (8), 933.
46. Grosse, C.; Delgado, A., Dielectric dispersion in aqueous colloidal systems. *Current Opinion in Colloid & Interface Science* **2010,** *15* (3), 145-159.
47. Morgan, H.; Green, N. G., *AC electrokinetics*. Research Studies Press: 2003.
48. Wang, X.; Becker, F. F.; Gascoyne, P. R., Membrane dielectric changes indicate induced apoptosis in HL-60 cells more sensitively than surface phosphatidylserine expression or DNA fragmentation. *Biochimica et biophysica acta* **2002,** *1564* (2), 412-20.
49. Narayanan Unni, H.; Hartono, D.; Yue Lanry Yung, L.; Mah-Lee Ng, M.; Pueh Lee, H.; Cheong Khoo, B.; Lim, K.-M., Characterization and separation of Cryptosporidium and Giardia cells using on-chip dielectrophoresis. *Biomicrofluidics* **2012,** *6* (1), 012805.
50. Su, Y.-H.; Tsegaye, M.; Varhue, W.; Liao, K.-T.; Abebe, L. S.; Smith, J. A.; Guerrant, R. L.; Swami, N. S., Quantitative dielectrophoretic tracking for characterization and separation of persistent subpopulations of Cryptosporidium parvum. *Analyst* **2014,** *139* (1), 66-73.
51. Cruz, J.; Garcia-Diego, F. In *Dielectrophoretic force measurements in yeast cells by the Stokes method*, IAS'97. Conference Record of the 1997 IEEE Industry Applications Conference Thirty-Second IAS Annual Meeting, IEEE: 1997; pp 2012-2018.
52. Zhang, Y.; Chen, X., Dielectrophoretic microfluidic device for separation of red blood cells and platelets: a model-based study. *Journal of the Brazilian Society of Mechanical Sciences and Engineering* **2020,** *42* (2), 89.

53. Huang, Y.; Wang, X.-B.; Becker, F. F.; Gascoyne, P. R., Membrane changes associated with the temperature-sensitive P85gag-mos-dependent transformation of rat kidney cells as determined by dielectrophoresis and electrorotation. *Biochimica et Biophysica Acta (BBA)-Biomembranes* **1996,** *1282* (1), 76-84.
54. Liang, W.; Zhao, Y.; Liu, L.; Wang, Y.; Li, W. J.; Lee, G.-B., Determination of cell membrane capacitance and conductance via optically induced electrokinetics. *Biophysical journal* **2017,** *113* (7), 1531-1539.
55. Pethig, R.; Talary, M., Dielectrophoretic detection of membrane morphology changes in Jurkat T-cells undergoing etoposide-induced apoptosis. *Iet Nanobiotechnology* **2007,** *1* (1), 2-9.
56. Heldt, C. L.; Hernandez, R.; Mudiganti, U.; Gurgel, P. V.; Brown, D. T.; Carbonell, R. G., A colorimetric assay for viral agents that produce cytopathic effects. *J Virol Methods* **2006,** *135* (1), 56-65.
57. van Dooren, B. T.; Beekhuis, W. H.; Pels, E., Biocompatibility of trypan blue with human corneal cells. *Archives of ophthalmology* **2004,** *122* (5), 736-742.
58. An, R.; Massa, K.; Wipf, D. O.; Minerick, A. R., Solution pH change in non-uniform alternating current electric fields at frequencies above the electrode charging frequency. *Biomicrofluidics* **2014,** *8* (6), 064126.
59. An, R.; Wipf, D. O.; Minerick, A. R., Spatially variant red blood cell crenation in alternating current non-uniform fields. *Biomicrofluidics* **2014,** *8* (2), 021803.
60. Larsen, R. D., Box-and-whisker plots. *Journal of Chemical Education* **1985,** *62* (4), 302.
61. De Myttenaere, A.; Golden, B.; Le Grand, B.; Rossi, F., Mean absolute percentage error for regression models. *Neurocomputing* **2016,** *192*, 38-48.
62. Adams, T.; Turner, P.; Janorkar, A.; Zhao, F.; Minerick, A., Characterizing the dielectric properties of human mesenchymal stem cells and the effects of charged elastin-like polypeptide copolymer treatment. *Biomicrofluidics* **2014,** *8* (5), 054109.
63. Strober, W., Trypan blue exclusion test of cell viability. *Current protocols in immunology* **1997,** *21* (1), A. 3B. 1-A. 3B. 2.
64. Buja, L.; Eigenbrodt, M. L.; Eigenbrodt, E. H., Apoptosis and necrosis. Basic types and mechanisms of cell death. *Archives of pathology & laboratory medicine* **1993,** *117* (12), 1208-1214.
65. Zhang, H.; Huang, Y.; Du, Q.; Luo, X.; Zhang, L.; Zhao, X.; Tong, D., Porcine parvovirus infection induces apoptosis in PK-15 cells through activation of p53 and mitochondria-mediated pathway. *Biochemical and biophysical research communications* **2015,** *456* (2), 649-55.
66. Gulati, G. L., *Blood Cell Morphology: Grading Guide*. American Society for Clinical Pathology Press Chicogo, IL: 2009.
67. Trägner, D.; Csordas, A., Biphasic interaction of Triton detergents with the erythrocyte membrane. *The Biochemical journal* **1987,** *244* (3), 605-609.
68. Rasia, M.; Bollini, A., Red blood cell shape as a function of medium's ionic strength and pH. *Biochimica et Biophysica Acta (BBA)-Biomembranes* **1998,** *1372* (2), 198-204.
69. Fischer, T. M., Shape memory of human red blood cells. *Biophys J* **2004,** *86* (5), 3304-13.
70. Tsong, T. Y.; Kingsley, E., Hemolysis of human erythrocyte induced by a rapid temperature jump. *Journal of Biological Chemistry* **1975,** *250* (2), 786-789.
71. Minerick, A. R.; Collins, J. L.; Leonard, K. M.; Adams, T. N., Methods and systems for identifying a particle using dielectrophoresis. Google Patents: 2018.
72. Zink, D.; Sadoni, N.; Stelzer, E., Visualizing chromatin and chromosomes in living cells. *Methods* **2003,** *29* (1), 42-50.